Hydrothermal synthesis of CeO$_2$ nanostructures and their electrochemical properties

A. N. Bugrov[1,2], V. K. Vorobiov[1], M. P. Sokolova[1], G. P. Kopitsa[3,4], S. A. Bolshakov[2], M. A. Smirnov[1]

[1]Institute of Macromolecular Compounds RAS, Bolshoy pr. 31, 199004 St. Petersburg, Russia
[2]St. Petersburg Electrotechnical University "LETI", ul. Professora Popova 5, 197376 St. Petersburg, Russia
[3]Grebenshchikov Institute of Silicate Chemistry RAS, Makarova emb. 2., letter B, 199034 St Petersburg, Russia
[4]St. Petersburg Nuclear Physics Institute, NRC KI, Orlova roscha mcr. 1, 188300 Gatchina, Leningrad region, Russia

alexander.n.bugrov@gmail.com, vrbvrbvrb@mail.ru, pmarip@mail.ru, kopitsa@mail.pnpi.spb.ru,
sergey_bolshakov01@mail.ru, smirnov_michael@mail.ru

Functional nanomaterials based on transition metal oxides are often used for the manufacture of supercapacitors and batteries, due to their special redox properties. The nanosized transition metal oxides used as the electrode material in some cases exhibit abnormally high values of capacitance and energy density. In this regard, it is important to understand what structural features of the nanomaterial determine the electrochemical characteristics of an electronic device. For this purpose, ceria nanorods and nanocubes were specifically synthesized under hydrothermal conditions at elevated pressure (15 MPa), different alkali contents, and two temperature regimes (100 and 180 °C). The obtained CeO$_2$ nanostructures were characterized using the methods of X-ray diffraction, transmission electron microscopy, and low-temperature nitrogen adsorption. The electrochemical properties of ceria nanostructures were investigated in 1 M Na$_2$SO$_4$ water electrolyte. The influence of the structural and surface characteristics of the synthesized nanorods and nanocubes on their charge storage ability is discussed. It was shown that CeO$_2$ in the form of nanocubes demonstrate higher specific capacitance in comparison with nanorods, which makes them more attractive for application in supercapacitors with neutral electrolytes.

Keywords: cerium dioxide, hydrothermal method, nanorods, nanocubes, fluorite structure, specific surface area, cyclic voltammetry, specific capacitance.

Received: 12 December 2019

Revised: 9 January 2020

1. Introduction

Inorganic oxides and composites based on them with electroconducting polymers or carbon nanomaterials attract increased attention as prospective materials for electrochemical energy storage devices due to their capability to store charge via reversible redox reactions. In a number of recent works, the electrochemical properties of supercapacitor electrode materials containing MnO$_2$ [1], WO$_3$ [2], Fe$_3$O$_4$ [3], Mn$_3$O$_4$ [4], RuO$_2$ [5], MoO$_3$ [6] or Fe$_2$O$_3$ [7] were reported. Ceria (CeO$_2$) is also one of the widely investigated prospective candidate [8]. In ceria structure, each Ce^{4+} cation is coordinated by eight neighboring oxygen anions, which occupy octahedral interstitials surrounded by four cerium atoms [9]. Fluorite-structured CeO$_2$, as a rule, contains internal Schottky and Frenkel defects caused by thermal motion in crystals and equilibrium reactions with gaseous oxygen in the environment [10]. At low oxygen partial pressure and elevated temperatures, Ce^{4+} can spontaneously reduce to the trivalent state, creating both oxygen vacancies and quasi-free localized electrons in the ceria crystal lattice [11, 12]. Oxygen non-stoichiometry of CeO$_2$ substantially determines its electrochemical [13], but does not have any complex mechanism that causes phase transformation and structural symmetry changes like in zirconia [14, 15]. The low redox potential of transition between Ce^{4+} and Ce^{3+}, along with the high mobility of oxygen in the crystalline structure of CeO$_2$, leads to the manifestation of mixed ion-electron conductivity. The ability to accumulate and release oxygen as a result of reversible redox transitions of Ce^{4+}/Ce^{3+} valence states causes CeO$_2$ to be used as a promoter in three-component catalysts for removing toxic exhaust gases [16], as a regulator of the thermal properties of polymers [17], a solid oxide fuel cell [18], an antioxidant [19] and anode material in lithium-ion batteries [20].

It is known that the concentration of oxygen defects increases with decreasing particle size of ceria, as well as with the transition from zero- to the one-dimensional nanostructures [21, 22]. An increase in the number of point defects is observed in a series of nanoscale rods ¿ cubes ¿ octahedra [22]. Usually, three planes (100), (110) and (111) go out onto the surface of ceria nanostructures. The formation energy of oxygen vacancies in the {111} facets is higher than in the {110} and {100} ones [23]. The growth directions of CeO$_2$ crystals and the type of planes forming their surfaces can be controlled by varying the synthesis conditions [24, 25]. In the case of nanosized octahedra, eight (111) and six (100) planes go outside, while CeO$_2$ cubes are usually surrounded by six {100} facets. The situation is much more complicated for nanorods since they can grow both 1) along the [110] direction with the exposure of the {100} and {110} facets, and 2) along [211], [111], [102] and [100] directions, which open the {111} and

$\{110\}$ facets to the surface [26]. Moreover, the specific surface area of one-dimensional structures is usually higher than that of cubes and octahedra. According to published data, the defectiveness and the ratio of the surface area to volume for CeO_2 nanostructures are decisive not only in terms of catalytic [27] and biological properties [28–30], but also in electrochemical characteristics. The higher specific electrochemical capacitance for nanorods (162.47 F g^{-1}) compared to nanoscale octahedra and cubes in alkali electrolyte (3 M KOH) was reported [31]. This result was attributed simultaneously to the high surface area of nanorods and to the predominant effect of $\{110\}$ and $\{100\}$ facets. For the case of ceria electrochemical properties in eco-friendliy neutral electrolyte it was demonstrated that increasing of amount of surface defects leads to an increase in electrochemical capacitance [32]. At the same time, the electrochemical performance in neutral electrolyte can also be influenced by crystalline facets exhibited on the surface of ceria nanoparticles and this point was not discussed yet.

Therefore, the aim of this study was to investigate the electrochemical performance of CeO_2 nanoparticles in a neutral electrolyte and to compare the electrochemical charge storage ability of ceria nanorods, the contact surface of which is represented by $\{110\}$ / $\{111\}$ facets with nanocubes surrounded exclusively by $\{100\}$ ones. To this end, ceria nanostructures of the above morphology were obtained under hydrothermal conditions. The structure of nanoparticles and their electrochemical charge storage ability in 1 M Na_2SO_4 electrolyte were studied.

2. Experimental

2.1. Synthesis of ceria nanostructures

To obtain ceria nanostructures in the form of rods and cubes $Ce(NO_3)_3 \cdot 6H_2O$ (chemically pure, CAS 10294-41-4, Vekton, Russia) and sodium hydroxide (analytically pure, GOST 4328-77, Vecton, Russia) as a precipitant were used. A highly concentrated alkali solution (9 M for rods and 6 M for cubes) was added dropwise to a previously prepared 0.5 M solution of cerium(III) nitrate. Initially, a brown suspension formed, which after 30 minutes stirring at room temperature changed color to light yellow. The resulting suspension was transferred to an autoclave and treated under hydrothermal conditions for 24 hours at a pressure of 15 MPa and a temperature of 100 $^\circ$C to obtain one-dimensional nanostructures or 180 $^\circ$C in the case of crystallization of nanoscale cubes. After hydrothermal treatment, the obtained white precipitates of CeO_2 nanoparticles were repeatedly washed with distilled water and ethanol, followed by drying at 60 $^\circ$C in air for a day.

2.2. Instruments and characterization

The size, shape and structure of the ceria nano-objects obtained in this study were determined using a JEM-2100F (Jeol Ltd., Japan) transmission electron microscope at an accelerating voltage of 200 kV. Aqueous dispersions of CeO_2 nanopowders were deposited on copper grids coated with graphene to obtain bright-field images and electron microdiffraction patterns.

X-ray diffraction (XRD) patterns of CeO_2 nanostructures were obtained using a SmartLab 3 (Rigaku Corporation, Tokyo, Japan) diffractometer with CuK$_\alpha$ radiation. The scanning was conducted in the range of 2θ angles from 20 to 80°. To take into account the instrumental broadening, the Caglioti parameters established by fitting the complete profile of the diffraction pattern of the external LaB$_6$ standard in the MAUD program were used. The unit cell parameters of CeO_2 nanostructures were determined in the same software package using a crystallographic information file of ceria [33] from the COD database according to the procedure described in [34]. The average size of the coherent scattering regions for both nanoscale rods and cubes was calculated using the Scherrer equation.

The values of S_{BET} of the powders of CeO_2 nanorods and nanocubes were measured by low-temperature nitrogen adsorption using a Nova 4200V analyzer (QuantaChrome, USA). Before measurements, the samples were degassed at 150 $^\circ$C in vacuo for 16 hours. S_{BET} of the samples was calculated using the Brunauer–Emmett–Teller model by 7 points in the range of partial nitrogen pressures $P/P_0 = 0.07 - 0.25$. The pore size distribution was estimated on the basis of nitrogen desorption isotherms by the Barrett–Joyner–Halenda (BJH) method.

Fourier transform infrared (FTIR) spectroscopy study was performed on the IRAffinity-1S spectrometer (Shimadzu, Japan) in the range 350 – 4000 cm^{-1}. Spectra for CeO_2 nanopowders were measured in the transmission mode using KBr pellets.

The electrochemical properties of the synthesized nano-objects were tested in standard 3-electrode cells. The working electrodes were prepared by dispersion of ceria in the N,N-dimethylformamide (anhydrous, 99.8 %, CAS 68-12-2, Sigma-Aldrich) containing carbon black and poly(1,1-difluoroethylene) (PVDF; average $M_w = 1.9 \times 10^5$, Kynar-720®, Atofina Chemicals Inc., USA). The glass carbon electrode with working area 1.3 cm^2 was covered with 0.3 ml of prepared dispersion and dried at 60 $^\circ$C. As a result, the electrodes containing 1.5 mg of ceria nanoparticles, 0.2 mg of carbon black and 0.2 mg of PVDF as a binder were prepared. The Ag/AgCl electrode as a reference and

Pt foil as a counter electrode were used. 1 M Na$_2$SO$_4$ was used as an electrolyte. Experiments were conducted with P-40X potentiostat-galvanostat ("Elins", Moscow, Russia).

3. Results and discussion

Alkali concentration and hydrothermal treatment temperature were key factors in the formation of CeO$_2$ structures in the form of nanocubes and nanorods. CeO$_2$ nanosized rods with an average diameter of 10 nm and a length of 100 nm are formed according to transmission electron microscopy (TEM) in the case of using a 9 M NaOH solution as a hydrothermal medium at 100 °C and a pressure of 15 MPa after 24 hours (Fig. 1a, row 1). Weaker alkaline solutions reduce the anisotropy of ceria nanostructures, which crystallize under hydrothermal conditions, and increasing the temperature to 180 °C intensifies the dissolution/recrystallization processes and oxidation of the Ce(OH)$_3$ clusters to CeO$_2$ [25, 35]. The above processes contribute to the formation of nanoscale cubes, rather than nanorods (Fig. 1b, row 2). The CeO$_2$ nanocubes synthesized in a 6 M NaOH solution at an elevated temperature from cerium (III) hydroxide exhibit a wide particle size distribution ranging from 10 to 54 nm. The average nanocube size was 38 nm, in accordance with the statistics collected on the base of 15 TEM micrographs. The rings in the microdiffraction patterns of both nanorods and nanocubes corresponding to the diffraction planes (111), (200), (220), (311), (222), (400), (331), (420) confirm their cubic crystalline lattice (Fig. 1b).
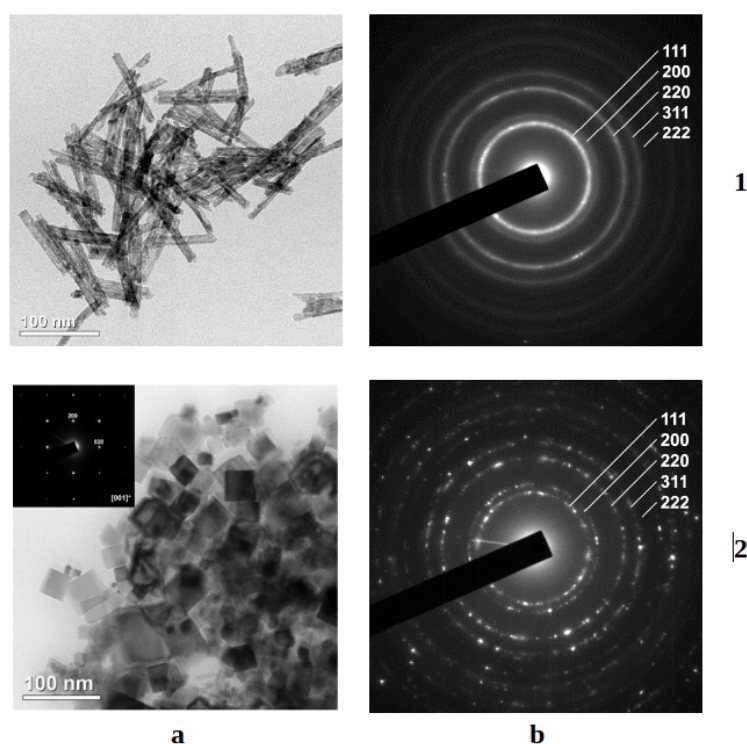

FIG. 1. TEM micrographs (a) and electron microdiffraction patterns (b) of CeO$_2$ nanorods (1) and nanocubes (2) obtained under hydrothermal conditions with varying pH and synthesis temperature

The surface structure of CeO$_2$ nanoparticles was investigated with high-resolution transmission electron microscopy (HRTEM), images for nanocubes and nanorods are given in Fig. 2a and Fig. 2b,c, respectively. The obtained results confirm that nanocubes exhibit {100} facets on the surface, while {110} and {111} facets are characteristic for nanorods. On the base of this data the 3D models of CeO$_2$ crystallites with the relevant top surfaces (Fig. 2b, e, h) and the projections of atoms positions on the plane which is perpendicular to the surface (Fig. 2c, f, i) were built. These projections clearly demonstrate the distance between the surface and neighboring Ce^{4+} ions for the different types of crystalline facets. The maximal distance is observed for {100} facet (0.14 nm), while for {111} facet this value is 0.08 nm. In the case of {110} facet, Ce^{4+} ions appear on the surface. These data allow one to propose that adsorption of sodium ions from electrolyte on {100} facet is favorable in comparison with {110} and {111} facets due to lower electrostatic repulsion between Ce^{4+} and Na$^+$ ions. As a result, the highest electrical capacitance can be expected for the {100} surface, which is in agreement with results of electrochemical measurements presented below.
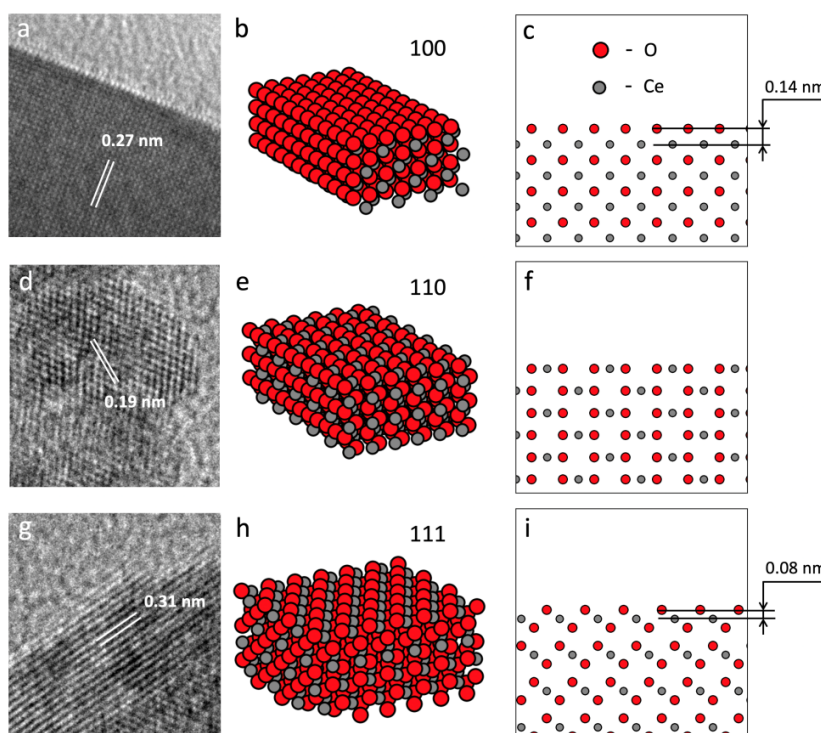
FIG. 2. HRTEM images for surfaces of the CeO_2 nanostructures (a, d, g), 3D model perspectives (b, e, h) and projections on the plane perpendicular to the surface (c, f, i) for nanocubes (a – c) and nanorods (d – i)

The XRD patterns of the synthesized CeO_2 nanostructures are shown in Fig. 3. The XRD analysis performed using the PD-Win 4.0 software package revealed the complete correspondence of nanoscale rods and cubes to the fluorite structure with the Fm3m space group (Card No. 43-1002 according to the ASTM database [36]). The average size of the coherent scattering regions for CeO_2 nanorods, calculated using the Scherrer equation for broadening of the XRD peaks, was 9 ± 1 nm (Fig. 3a). The crystallite size for cubic nanoparticles was larger, approximately 40 nm (Fig. 3b). Compared to CeO_2 nanocubes, the unit cell parameters calculated for nanorods were higher due to a greater number of structural defects, the evolution of distortions and stresses in crystallites [37] (Table 1).

TABLE 1. X-ray diffraction data for prepared ceria nanostructures

Morphology	Unit cell parameters			Average crystallite size, nm	Microstrain
	Lengths, Å	Angles, °	V, Å³		
Nanorods	$a = b = c = 5.427$	$\alpha = \beta = \gamma = 90$	159.8	9 ± 1	$2.73 \cdot 10^{-3}$
Nanocubes	$a = b = c = 5.414$	$\alpha = \beta = \gamma = 90$	158.7	40 ± 3	$2.86 \cdot 10^{-8}$

According to the data of low-temperature nitrogen adsorption, the porosity and S_{BET} of ceria nanopowders substantially depend on the morphology of structures formed during hydrothermal treatment, their imperfection, and size. Fig. 4 shows the complete adsorption-desorption isotherms for CeO_2 powders of nanorods and nanocubes. Both measured isotherms are characterized by a rather narrow capillary-condensation hysteresis and are of type IV according to the IUPAC classification. This type corresponds to adsorption on mesoporous materials. The hysteresis loop can be classified as type H3, which is characteristic of materials with slit-like pores. Estimates of the S_{BET} are presented in Table 2 and indicate a significant decrease in its value from 108.2 to 18.5 m^2/g during the transition from CeO_2 nanorods to nanocubes. This fact is in good agreement with the XRD data and electron microscopy, according to which the crystallite size decreases and the fraction of oxygen vacancies in them increases, contributing to the formation of a more developed surface (Fig. 1, Table 1).
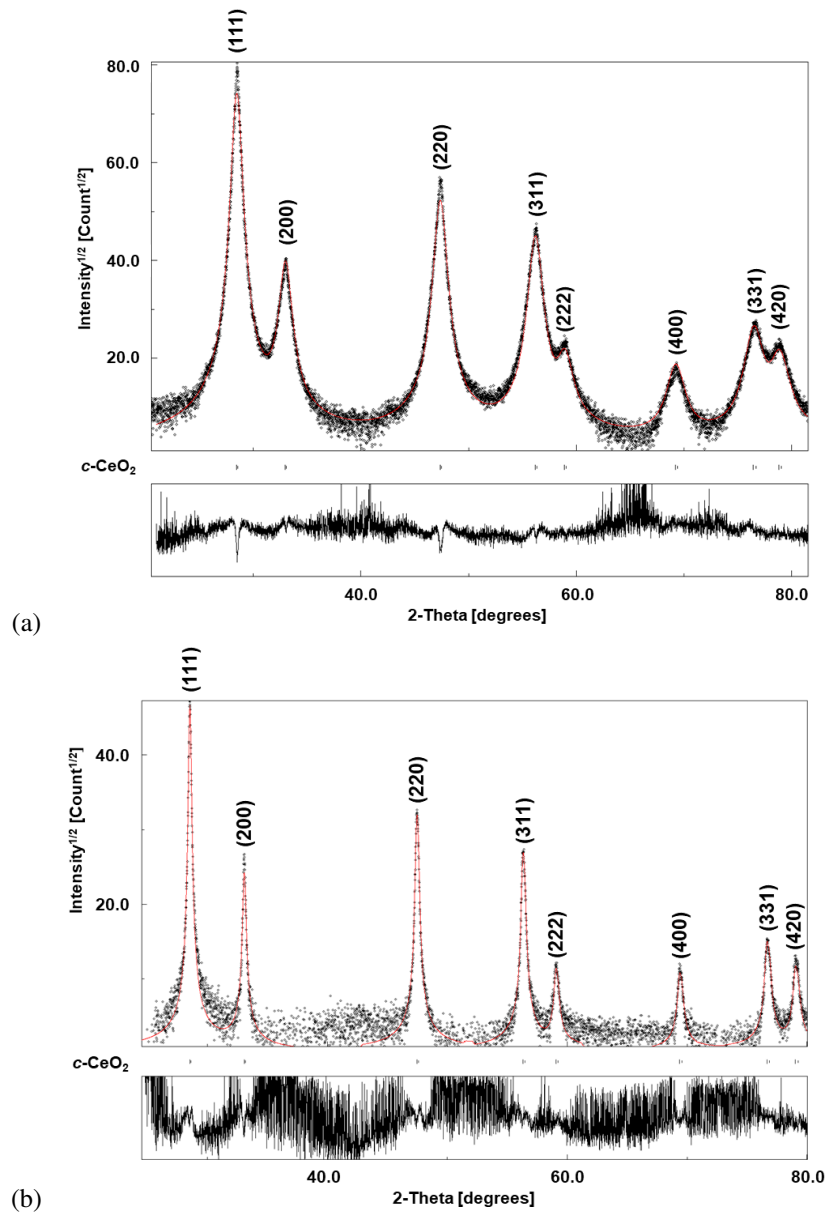
(a)

(b)

FIG. 3. XRD patterns of CeO$_2$ nanorods (a) and nanocubes (b) obtained under hydrothermal conditions with varying pH and temperature of the synthesis

TABLE 2. The structural parameters determined by the method of low-temperature nitrogen adsorption for prepared CeO$_2$ nanoparticles

Morphology	S_{BET}, m^2/g	D_1, nm	D_2, nm	V_{pores}^*, cm^3/g
Nanorods	108.2 ± 2.2	2.4	13.2	0.43
Nanocubes	18.5 ± 2.8	1.9	36.4	0.22

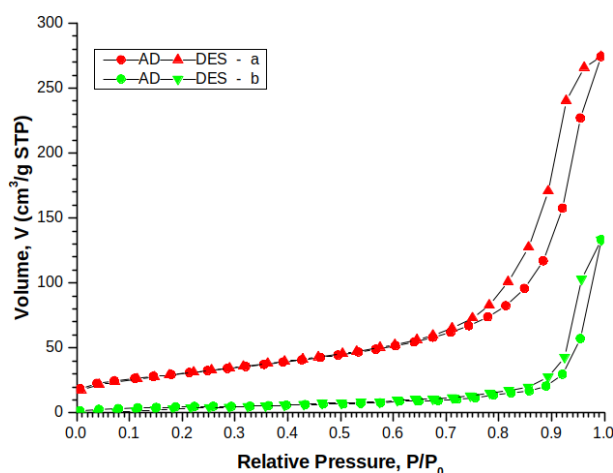* The specific pore volume is determined by the maximum filling ($P/P_0 = 0.99$).

FIG. 4. Adsorption (AD)-desorption (DES) isotherms for CeO_2 nanorods (a) and nanocubes (b) obtained under hydrothermal conditions with varying pH and temperature of the synthesis

The pore size distributions calculated from the desorption branch of isotherm by the BJH algorithm for nanorod and nanocube powders are shown in Fig. 5. Both types of synthesized CeO_2 nanostructures are characterized by a bimodal pore size distribution. Micropores are formed as a result of the splicing of nanocrystallites by the mechanism of oriented attachment, and mesopores are the result of their subsequent aggregation [38]. The position of the second maximum (D_2) for nanocubes is substantially (about 3 times) shifted toward larger pore sizes in comparison with nanorods (Table 2). The specific pore volume for nanostructures with a minimum axial ratio, on the contrary, decreases from 0.43 to 0.22 cm^3/g due to dense crystallite compaction.
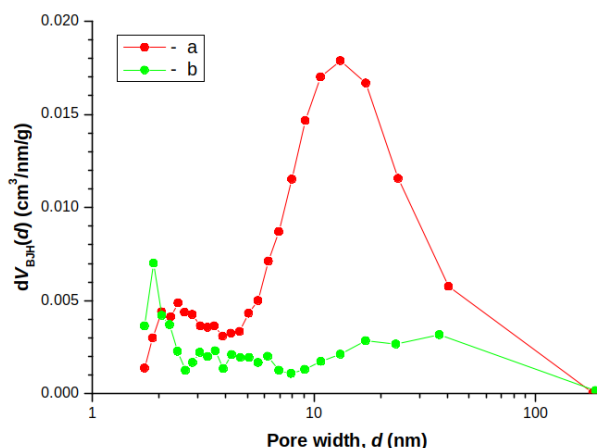

FIG. 5. Pore size distributions for CeO_2 nanorods (a) and nanocubes (b), calculated by the BJH algorithm

FTIR analysis was carried out to take into account possible effect of the surface hydroxylation degree of CeO_2 nanostructures formed under different conditions of hydrothermal synthesis on the electrochemical properties of electrodes. It is known that surface hydroxyl groups can influence the electrochemical performance of inorganic electrodes. For example, significant increase of specific capacitance of MoO_3 nanowires was observed after its hydrogenation [39]. The authors mention that along with increasing of electrical conductivity, the increasing of density of surface hydroxyl groups can be the factor that increases the specific capacitance.

However, the mechanism of influence for surface hydroxylation on the capacitance properties of metal oxides is not clear. It can be proposed that if hydrogen is involved in electrochemical process, surface hydroxylation can promote the reaction. This was demonstrated for electrochemical reduction of CO_2 on the surface of tin oxide [40]. The increasing of electrical current during CV cycling for WO_3 in acidic electrolyte was also observed [41].

The FTIR spectra of CeO_2 nanostructures obtained in this work are given in Fig. 6. The following bands corresponding to surface OH groups can be found within the $3800 - 3000$ cm^{-1} region of FTIR spectra in the case of CeO_2 synthesized under hydrothermal conditions at high pH: isolated (3700 cm^{-1}), bridging (3641 cm^{-1}), multiple bonded

(3550 – 3500 cm^{-1}) and hydrogen bridging hydroxyls (wide band around 3400 cm^{-1}) [42, 43]. It is seen in Fig. 6a and 6b, that in our case these bands overlap forming one wide peak 3700 – 3000 cm^{-1} centered near 3447 cm^{-1} for both prepared samples. The relative number of surface hydroxyls can be estimated from the maximum of intensity of the band centered at 3447 cm^{-1} (I$_{3447}$) after normalization of the spectra according to the intensity of Ce–O stretching vibration peak (around 430 cm^{-1}). The found values of I$_{3447}$ were 0.080 and 0.414 for nanocubes and nanorods, respectively (ratio nanorods:nanocubes = 5.2). Taking into account the ratio between the specific surface of nanorods and nanocubes (5.8), the slightly higher surface density of hydroxyl groups for nanocubes in comparison to nanorods can be proposed. However, the difference is rather small (about 12 %) thus, it can be assumed that for our experiment the type of exhibited crystallographic plane will be the main parameter that leads to the difference in the electrochemical performance between nanorods and nanocubes.
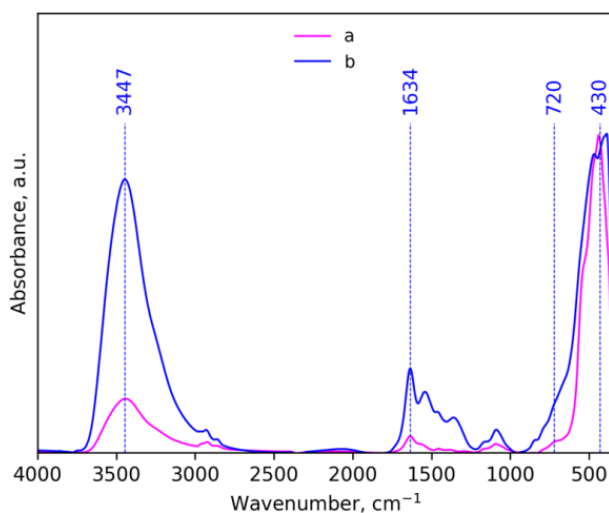

FIG. 6. FTIR spectra of CeO$_2$ nanocubes (a) and nanorods (b), normalized to a band of 430 cm^{-1}

The absorption bands for the 1250 – 850 cm^{-1} region in the FTIR spectra of CeO$_2$ nanocubes and nanorods can be attributed to the deformation vibrations of formates or carbonates formed due to the interaction of the surface of ceria nanostructures with atmospheric CO$_2$. Signals in the 2800 – 2900 cm^{-1} range correspond to stretching vibrations of C–H groups, and the bands at 1634 and 720 cm^{-1} are deformation vibrations of O–H and stretching vibrations of Ce–O–Ce groups, respectively.

The capacitance properties of CeO$_2$ nanostructures were investigated with cyclic voltammetry (CV) and galvanic charge-discharge (GCD) measurements. The CV curves of ceria nanostructures with different morphology were measured at a scan rate of 10 mV/s in the potential range $-0.2 - +0.5$ V vs Ag/AgCl reference electrode. The results shown in Fig. 7a demonstrate that ceria in the form of cubes has significantly higher area covered with CV curve in comparison with CeO$_2$ nanorods. This means higher capacitance of electrode material containing CeO$_2$ nanocubes, which agrees with GCD curves given in Fig. 7b. GCD curves demonstrate slightly disturbed triangular shape, which is characteristic for capacitive behavior of the material. Non-ideal triangular shape in the connection with waves on CV curves gives evidence that pseudocapacitance mechanism of charge storage also takes place. The specific capacitance (C_{GCD}) of electrodes was calculated form GCD experiments as:

$$C_{\text{GCD}} = \frac{It}{A(U_2 - U_1)},$$

where I – applied current, t – discharge time, A – electrode area, U_2 and U_1 are the upper and the lower limits of the voltage range.

Values of C_{GCD} for CeO$_2$ in the form of nanocubes and nanorods found using this equation are 5.7 and 0.59 mF/cm^2, respectively. Since the specific surface for nanorods is significantly higher than that of nanocubes, it can be suggested that the difference in capacitance is connected with crystalline structure of the surface of nanoparticles. As it was mentioned earlier, depending on the conditions of hydrothermal synthesis, various directions of crystal growth and exposing of CeO$_2$ planes can be realized. In addition, the possibility of the transformation of the {110} and {100} exposed facets into {111} for nanorods obtained under hydrothermal conditions during their subsequent heat treatment was reported [44, 45]. In our case, growth of one-dimensional ceria structures through the [211] direction with exposed {111} and {110} facets takes place. As a result of a careful analysis of the changes in the morphology
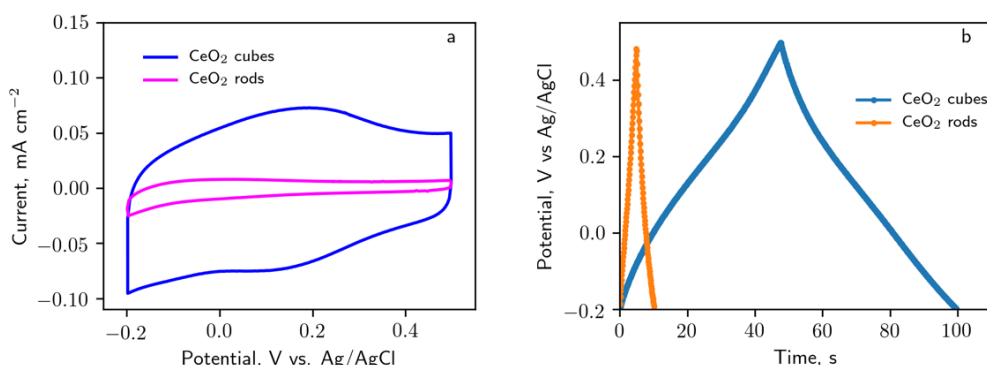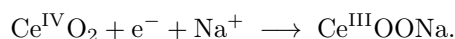
FIG. 7. Cyclic voltammetry curves measured at 10 mV/s (a) and galvanostatic charge-discharge curves measured at 0.08 mA/cm^2(b)

of CeO$_2$ nanorods at different stages of hydrothermal synthesis, prior authors [28] found that one-dimensional structures with orientation along the [211] direction are formed by the so-called "oriented attachment" mechanism. The driving force for this spontaneously oriented attachment is a decrease in the total surface energy due to the union of the planes by means of which the crystals are joined. The attachment can take place either along the [211] direction with exposed {111} facets or along the [110] direction with {200} facets exposure [46]. The former would be more favorable because the CeO$_2$ {111} surface is the most stable one. The formation of nanorods along the [211] direction via oriented attachment followed by Ostwald ripening under the conditions of hydrothermal synthesis applied in this work was observed in contrast to [25]. This fact is supported with the significantly lower electrochemical activity of nanorods in the electrochemical experiment. The mechanism, proposed for the charge storage process in ceria, takes into account the adsorption of cation from electrolyte on the surface of crystal [31]. At the next stage, the reduction of cerium (IV) to cerium (III) can occur, leading to the realization of pseudocapacitance in the electrode [47]. These two stages can be summarized as follows:

$$Ce^{IV}O_2 + e^- + Na^+ \longrightarrow Ce^{III}OONa.$$

As it was demonstrated earlier, among the most common surface planes of ceria, exactly (100) is characterized with the highest projection of distance between cerium and oxygen atoms on the axis perpendicular to the surface of the nanocrystal. Thus, the possibility of most negative surface potential can be proposed for (100) plane in comparison with others. This can lead to the enhancement of Na$^+$ adsorption on the surface presented with this plane.

For further investigation of capacitance properties of CeO$_2$ nanocubes, the contributions of two different mechanisms of charge storage: i.e., capacitance of "outer" active surface and capacitance connected with the ion insertion process (capacitance of the "inner" active surface) were estimated according to the method developed by Trasatti [48]. This method is based on the analysis of variation of electrode capacitance on the scan rate during CV experiments. The corresponding CV measurements in the range of scan rates from 1 up to 20 mV/s are given in Fig. 8a. The capacitance values, calculated from given results, are plotted versus the square root of the reciprocal scan rate (Fig. 8b) and the reciprocal capacitance – versus the square root of the scan rate (Fig. 8c). Linear extrapolation of both plots to $x = 0$ gives the values of the "outer" surface and total theoretical (C_{total}) capacitances of the material, respectively. The "outer" surface capacitance, which is scan-rate independent can be considered as the double-layer-like capacitance (C_{dl}). The value of C_{total} includes both the "inner" and "outer" surface capacitances. The "scan-rate dependent" capacitance of "inner" surface can be considered as a pseudocapacitance-like (C_{p}) one, which, in our case, can be connected with an oxidation/reduction transition between Ce^{4+} and Ce^{3+} accompanied with insertion/release of sodium ions. The value of C_{p} can be calculated as $C_{\text{p}} = C_{\text{total}} - C_{\text{dl}}$.

As it is seen from Fig. 8b and c, the values of C_{dl} and C_{total} for CeO$_2$ nanocubes are 4.7 and 7.7 mF cm^{-2}, respectively. The value of capacitance, obtained from GCD measurements (5.7 mF/cm^2) is between C_{dl} and C_{total}, which is the reasonable result. This allows to propose that 61 % of CeO$_2$ capacitance is connected with charge-discharge of electrochemical double layer, while only 39 % is provided by pseudocapacitance-like mechanism. It worth mentioning that, both mechanisms of charge storage are closely connected with the adsorption of cations from solution onto the surface of nanoparticles. Thus, the structural characteristics of ceria's surface are of prime importance for its capacitance properties.
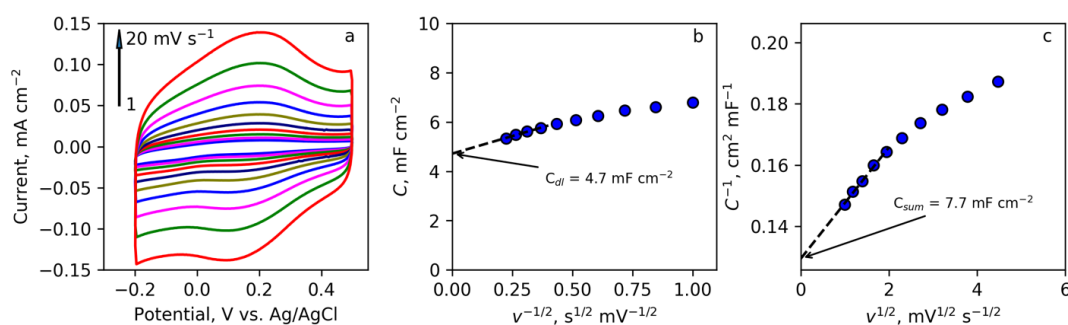
FIG. 8. Cyclic voltammetry curves for CeO$_2$ nanocubes at different scan rates (a), capacitance dependence on the square root of the reciprocal scan rate (b), and the reciprocal capacitance dependence on the square root of scan rate (c)

4. Conclusions

It was revealed using XRD, TEM, HRTEM that ceria nanorods are formed from the CeO$_2$ nucleating centers along the [211] direction with inactive {111} facets exposure by the attachment mechanism followed by Oswald ripening during hydrothermal synthesis at 100 °C. An increase in the synthesis temperature leads to the formation of CeO$_2$ nanocubes, with surface represented exclusively by {100} facets. It was demonstrated that despite the lower specific surface area, the capacitance of the CeO$_2$ nanocubes is 10 times higher than one for nanorods. It was suggested that this result is connected with the possibility of more favorable adsorption of cations onto {100} facets in comparison with those of {110} and {111}. Investigation of mechanism of charge storage using Trasatti method allows to assume that 61 % of total capacitance of CeO$_2$ nanocubes is realized via charging of double-layer, while 39 % can be attributed to the pseudocapacitance-like processes. The obtained results can be significant for further elaboration of polymer-inorganic composites based on CeO$_2$ for application in electrochemical devices and electrodes.

Acknowledgements

References

[1] Ivanova A.G., Karasev L.V., et al. Development and research of electroactive pseudocapacitor electrode pastes based on MnO$_2$. *Glass Physics and Chemistry*, 2020, **46** (1), P. 96–101.

[2] Zhuzhelskii D.V., Tolstopjatova E.G., et al. Electrochemical properties of PEDOT/WO$_3$ composite films for high performance supercapacitor application. *Electrochemica Acta*, 2019, **299**, P. 182–190.

[3] Nawwar M., Poon R., et al. High areal capacitance of Fe$_3$O$_4$-decorated carbon nanotubes for supercapacitor electrodes. *Carbon Energy*, 2019, **1**, P. 124–133.

[4] Ata M.S., Milne J., Zhitomirsky I. Fabrication of Mn$_3$O$_4$–carbon nanotube composites with high areal capacitance using cationic and anionic dispersants. *Journal of Colloid and Interface Science*, 2018, **512**, P. 758–766.

[5] Asim S., Javed M.S., et al. RuO$_2$ nanorods decorated CNTs grown carbon cloth as a free standing electrode for supercapacitor and lithium ion batteries. *Electrochimica Acta*, 2019, **326**, P. 135009.

[6] Ahmed S. Etman A.S., Wang Z., et al. Flexible freestanding MoO$_{3-x}$–carbon nanotubes–nanocellulose paper electrodes for charge-storage applications. *ChemSusChem*, 2019, **12**, P. 5157–5163.

[7] Yang Z., Tang L., et al. Hierarchical nanostructured α-Fe$_2$O$_3$/polyaniline anodes for high performance supercapacitors. *Electrochimica Acta,* 2018, **269** (10), P. 21–29.

[8] Khan A.J., Hanif M., et al. Energy storage properties of hydrothermally processed nanostructured porous CeO$_2$ nanoparticles. *Journal of Electroanalytical Chemistry*. 2020, **865**, P. 114158.

[9] He L., Su Y., Jiang L., Shi S. Recent advances of cerium oxide nanoparticles in synthesis, luminescence and biomedical studies: A review. *Journal of Rare Earths*, 2015, **33** (8), P. 791–799.

[10] Younis A., Chu D., Li S. Cerium oxide nanostructures and their applications. *Functionalized Nanomaterials*, 2016, **3**, P. 53–68.

[11] Ivanov V.K., Baranchikov A.E., et al. Oxygen nonstoichiometry of nanocrystalline ceria. *Russian Journal of Inorganic Chemistry*, 2010, **55** (3), P. 325–327.

[12] Kabir A., Zhang H., Esposito V. Mass diffusion phenomena in cerium oxide. In S. Scirè, & L. Palmisano (Eds.), *Cerium Oxide (CeO$_2$): Synthesis, Properties and Applications*, 2019, **5**, P. 169–210.

[13] Mogensen M., Sammes N.M., Tompsett G.A. Physical, chemical and electrochemical properties of pure and doped ceria. *Solid State Ionics*, 2000, **129** (1–4), P. 63–94.

[14] Bugrov A.N., Almjasheva O.V. Effect of hydrothermal synthesis conditions on the morphology of ZrO_2 nanoparticles. *Nanosystems: Physics, Chemistry, Mathematics*, 2013, **4** (6), P. 810–815.

[15] Bugrov A.N., Smyslov R.Yu., Zavialova A.Yu., Kopitsa G.P. The influence of chemical prehistory on the structure, photoluminescent properties, surface and biological characteristics of $Zr_{0.98}Eu_{0.02}O_{1.99}$ nanophosphors. *Nanosystems: Physics, Chemistry, Mathematics*, 2019, **10** (2), P. 164–175.

[16] Trovarelli A. Catalytic properties of ceria and CeO_2-containing materials. *Catalysis Reviews – Science and Engineering*, 1996, **38** (4), P. 439–520.

[17] Nikolaeva A.L., Gofman I.V., et al. Interplay of polymer matrix and nanosized Redox dopant with regard to thermo-oxidative and pyrolytic stability: CeO_2 nanoparticles in a milieu of aromatic polyimides. *Materials Today Communications*, 2020, **22**, P. 100803.

[18] Omar S., Wachsman E.D., Nino J.C. Higher ionic conductive ceria-based electrolytes for solid oxide fuel cells. *Applied Physics Letters*, 2007, **91** (14), P. 144106.

[19] Dhall A., Self W. Cerium oxide nanoparticles: A brief review of their synthesis methods and biomedical applications. *Antioxidants*, 2018, **7** (97), 13 p.

[20] Zhou F., Zhao X., Xu H., Yuan C. CeO_2 spherical crystallites: Synthesis, formation mechanism, size control, and electrochemical property study. *Journal of Physical Chemistry C*, 2007, **111** (4), P. 1651–1657.

[21] Deshpande S., Patil S., Kuchibhatla S.V., Seal S. Size dependency variation in lattice parameter and valency states in nanocrystalline cerium oxide. *Applied Physics Letters*, 2005, **87** (13), P. 133113.

[22] Wu Z., Li M., et al. Probing defect sites on CeO_2 nanocrystals with well-defined surface planes by Raman spectroscopy and O_2 adsorption. *Langmuir*, 2010, **26** (21), P. 16595–16606.

[23] Li C., Sun Y., et al. Shape-controlled CeO_2 nanoparticles: Stability and activity in the catalyzed HCl oxidation reaction. *ACS Catalysis*, 2017, **7** (10), P. 6453–6463.

[24] Tang W.-X., Gao P.-X. Nanostructured CeO_2: preparation, characterization, and application in energy and environmental catalysis. *MRS Communications*, 2016, **6** (4), P. 311–329.

[25] Mai H.-X., Sun L.-D., et al. Shape-selective synthesis and oxygen storage behavior of ceria nanopolyhedra, nanorods, and nanocubes. *Journal of Physical Chemistry B*, 2005, **109**, P. 24380–24385.

[26] Trovarelli A., Llorca J. Ceria catalysts at nanoscale: How do crystal shapes shape catalysis? *ACS Catalysis*, 2017, **7**, P. 4716–4735.

[27] Zhang D., Du X., Shi L., Gao R. Shape-controlled synthesis and catalytic application of ceria nanomaterials. *Dalton Transactions*, 2012, **41** (48). P. 14455–14475.

[28] Ji Z., Wang X., et al. Designed synthesis of CeO_2 nanorods and nanowires for studying toxicological effects of high aspect ratio nanomaterials. *ACS Nano*, 2012, **6** (6), P. 5366–5380.

[29] Popov A.L., Ermakov A.M., et al. Biosafety and effect of nanoparticles of CeO_2 on metabolic and proliferative activity of human mesenchymal stem cells in vitro. *Nanomechanics Science and Technology: An International Journal*, 2016, **7** (2), P. 165–175.

[30] Shcherbakov A.B., Zholobak N.M., Spivak N.Ya., Ivanov V.K. Advances and prospects of using nanocrystalline ceria in cancer theranostics. *Russian Journal of Inorganic Chemistry*, 2014, **59** (13), P. 1556–1575.

[31] Jeyaranjan A., et al. Morphology and crystal planes effects on supercapacitance of CeO_2 nanostructures: Electrochemical and molecular dynamics studies. *Particles and Particle Systems Characterization*, 2018, **35** (10), P. 1800176.

[32] Kumar M., Bhatt V., et al. Role of Ce^{3+} valence state and surface oxygen vacancies on enhanced electrochemical performance of single step solvothermally synthesized CeO_2 nanoparticles. *Electrochimica Acta*, 2018, **284**, P. 709–720.

[33] Ranjith K.S., Saravanan P., et al. Enhanced room-temperature ferromagnetism on co-doped CeO_2 nanoparticles: Mechanism and electronic and optical properties. *Journal of Physical Chemistry C*, 2014, **118** (46), P. 27039–27047.

[34] Lutterotti L., Pilliere H., et al. Full-profile search–match by the Rietveld method. *Journal of Applied Crystallography*, 2019, **52**, P. 587–598.

[35] Plakhova T.V., Romanchuk A.Yu., et al. Solubility of nanocrystalline cerium dioxide: Experimental data and thermodynamic modeling. *The Journal of Physical Chemistry C*, 2016, **120** (39), P. 22615–22626.

[36] Grier D., McCarthy G. ICDD Grant-in-Aid, North Dakota State University, Fargo, North Dakota, USA, 1991.

[37] Yan L., Yu R., Chen J., Xing X. Template-free hydrothermal synthesis of CeO_2 nano-octahedrons and nanorods: Investigation of the morphology evolution. *Crystal Growth & Design*, 2008, **8** (5), P. 1474–1477.

[38] Ivanov V.K., Polezhaeva O.S., et al. Specifics of high-temperature coarsening of ceria nanoparticles. *Russian Journal of Inorganic Chemistry*, 2009, **54** (11), P. 1689–1696.

[39] Shakir I., Shahid M., Rana A.U., Warsi F.M. In situ hydrogenation of molybdenum oxide nanowires for enhanced supercapacitors. *RSC advances*, 2014, **4** (17), P. 8741–8745.

[40] Cui C., Han J., et al. Promotional effect of surface hydroxyls on electrochemical reduction of CO_2 over SnO_x/Sn electrode. *Journal of catalysis*, 2016, **343**, P. 257–265.

[41] Yoshiike N., Kondo S. Electrochemical properties of $WO_3x(H_2O)$: I. The influences of water adsorption and hydroxylation. *Journal of The Electrochemical Society*, 1983, **130** (11), P. 2283–2287.

[42] Agarwal S., Lefferts L., Mojet B.L. Ceria nanocatalysts: Shape dependent reactivity and formation of OH. *ChemCatChem*, 2013, **5** (2), P. 479–489.

[43] Lypez J.M., Gilbank A.L., et al. The prevalence of surface oxygen vacancies over the mobility of bulk oxygen in nanostructured ceria for the total toluene oxidation. *Applied Catalysis B: Environmental*, 2015,**174–175**, P. 403–412.

[44] Ta N., Liu J., et al. Stabilized gold nanoparticles on ceria nanorods by strong interfacial anchoring. *Journal of the American Chemical Society*, 2012, **134** (51), P. 20585–20588.

[45] Wang S., Zhao L., et al. Morphology control of ceria nanocrystals for catalytic conversion of CO_2 with methanol. *Nanoscale*, 2013, **5** , P. 5582–5588.

[46] Ivanov V.K., Polezhaeva O.S., Tret'yakov Yu.D. Nanocrystalline ceria: Synthesis, structure-sensitive properties, and promising applications. *Russian Journal of General Chemistry*, 2010, **80** (3), P. 604–617.

[47] Maheswari N., Muralidharan G. Supercapacitor behaviour of cerium oxide nanoparticles in neutral aqueous electrolytes. *Energy Fuels*, 2015, **29**(12), P. 8246–8253.

[48] Ardizzone S., Fregonara G., Trasatti S. "Inner" and "outer" active surface of RuO_2 electrodes. *Electrochimica Acta*, 1990, **35** (1), P. 263–267.